Experimental Study on Time Evolution of Shock Wave and Turbulent Boundary Layer Interactions

X. G. Lu[†], S. H. Yi, L. He, X. L. Liu and F. Zhang

College of Aerospace Science and Engineering, National University of Defense Technology, No. 109, Deya Road, Changsha, Hunan, 410073, China

†*Corresponding Author Email: luxiaoge18@163.com*

ABSTRACT

In this paper, a test system based on the Nano-tracer Planar Laser Scattering (NPLS) technique for studying time evolution of unsteady flow structures was finished. Based on this system, the experimental study on the interactions between the incident shock wave and the turbulent boundary layer of the incoming wall was performed. The experiments were performed in a Mach 3.4 supersonic low-noise wind tunnel at the unit Reynolds number of $6.30 \times 10^6 / m^{-1}$. For the first time, five frames of temporal-correlated fine structure images of transient flow field with shock wave and the turbulent boundary layer interactions (SWTBLI) were obtained under the experimental conditions, and the spatiotemporal evolution characteristics of the flow structure were analyzed. At the same time, the flow field characteristics of temporal-correlated images were studied when the density boundary layer thickness of incoming turbulent layer is $\delta_1 = 0.55\delta$, $\delta_2 = 0.72\delta$, $\delta_3 = 0.87\delta$ respectively. During the development of vortex structure in the boundary layer from turbulent boundary layer to separation bubble, the oscillation interval distribution law of induced shock wave was summarized, and the group velocity of vortex structure development in the boundary layer and the relationship between boundary layer thickness and physical space size growth law of separation bubble under different incoming turbulent boundary layer thicknesses were obtained. The results also show that with the increase of the incoming boundary layer thickness, the group velocity in the development process of vortex structure in the turbulent boundary layer does not change significantly. As the thickness of the boundary layer entering the separation bubble increases, the overall growth height of the separation bubble also increases.

Keywords: Supersonic boundary layer; SWTBLI; NPLS; Temporal and spatial evolution characteristics.

NOMENCLATURE

h_i	height of the separation bubble	x_i	intersection point of the reverse extension lines of the induced shock wave and the x-axis
Ma_∞	Mach number of the supersonic low-noise wind tunnel		
P_0	total pressure		
Re	Reynolds number	Δt	interval time of temporal-correlated NPLS image
T_0	total temperature		
t	operation time of wind tunnel	β	shock angle
		θ	deflection angle of shock wave generator

1. INTRODUCTION

Shock wave and boundary layer interactions is a typical flow phenomenon widely existing in the external and internal flows of various supersonic or hypersonic aircrafts. The unsteady characteristics of shock wave and boundary layer interference are closely related to the Mach number, the characteristics of incoming boundary layer, the generation mode of shock wave, the intensity of incident shock wave, etc. Moreover, it has an important influence on the flight performance of supersonic or hypersonic aircrafts and has very important theoretical research value and engineering application background. In 1939, Ferri (1939) first discovered the phenomenon of shock wave and boundary layer interactions in wind tunnel experiments. Since then, the characteristics of shock

wave and boundary layer interactions have been extensively studied in the past eighty year. In many studies, the characteristics of shock wave and laminar boundary layer interactions have been relatively consistent. In contrast, shock wave and turbulent boundary layer interactions are more common, but their characteristics are more complex, and their flow mechanism is still not very clear. Donaldson and Du (1944), Liepmann (1946), Ackeret *et al.* (1947), and Fage and Sargent (1947) have revealed the importance of shock wave and boundary layer interactions by the wind tunnel tests and inviscid theoretical analysis. At the same time, it has been found that the characteristics of shock wave and boundary layer interactions under transonic conditions are closely related to the flow field structure of the incoming boundary layer (laminar boundary layer or turbulent boundary layer). Since the late 1940s, in the process of studying shock-induced boundary layer separation flow, Green (1970) used schlieren images to elaborate the flow field structure of shock wave and turbulent boundary layer interactions. Hankey and Holden (1975) and Adamson and Messiter (1980) made a preliminary summary of the previous researches on two-dimensional shock wave and boundary layer. Delery and Marvin (1986), Dolling (2001) and Smits and Dussauge (2006) reviewed the research results on unsteady and three-dimensional characteristics of shock wave and boundary layer. Since then, the research on shock wave and boundary layer interference has gradually entered the range of supersonic and hypersonic flow.

In recent years, with the rapid development of flow visualization techniques and the improvement of numerical simulation capability, the study of the shock wave and boundary layer interaction has also reached a new level. Researchers have paid more attention to the unsteady motion characteristics of shock wave and boundary layer interactions. Researches showed that large-scale coherent structures in boundary layer incoming flow have important influence on the unsteady characteristics of shock wave and boundary layer interaction. Tong *et al.* (2020) Studied the effect of changes in the location of the incident shock wave on the structure of the expansion zone through numerical simulation, and obtained that the change of the pulsation intensity of the separation bubble directly affects the dynamic characteristics in the expansion zone. John and Senthilkumar (2018) revealed through the present study that the blunt cowl leading edge can reduce the intensity of shock wave boundary layer interaction occurring at the isolator entry section. Wu and Martin (2008) have found that, the time scale of the low-frequency motion of the large-scale structure disturbed by shock wave and boundary layer was much larger than the characteristic time scale of the incoming boundary layer. Singh (2019) studied a laminar separation bubble is simulated by imposition of suction to create an adverse pressure gradient in DNS. Yao and Gao (2019) Established a theoretical prediction model for the separation characteristics of the boundary layer caused by the interference of the incident shock wave and the boundary layer. Using this theoretical model, the structure of the separation shock wave and the reattachment shock wave was simplified. The variation law of separation bubble height and incoming Mach number, external compression angle and flying height are obtained. Andreopoulos and Muck (1987) pointed out that the unsteady characteristics of shock wave and boundary layer interference are closely related to the characteristic frequency in the incoming boundary layer. Pirozzoli and Grasso (2006) used DNS method to study shock wave and boundary layer interference. They pointed out that the unsteady characteristics of large-scale structure in shock wave and boundary layer interference are related to noise feedback in incoming flow field. DuPont *et al.* (2006) studied shock wave and boundary layer interference through experiments and found that the low frequency motion of reflected shock wave was related to the law of separation bubble motion in interference region. Zhang *et al.* (2020) Summarized the interference characteristics and related research progress of simplified models of different types of interference phenomena for the phenomenon of shock waves and boundary layer interference flow that are common in high-speed intake ports.

NPLS technique is a fine flow field measurement technology, which is independently developed by the author's research group. It can get the fine structure of time evolution, which is convenient for the study of dynamics development process. And the NPLS technique is only possible to study the results in the measured profile, but not the time evolution of the entire three-dimensional structure. Zhao *et al.* (2007; 2008; 2009) applied NPLS technique to the experimental study of shock wave and boundary layer interactions for the first time, and observed the micro-scale structure in shock wave and boundary layer interactions flow field. He *et al.* (2011a; 2011b; 2017) and Lu *et al.* (2020) obtained the fine structure of the flow direction plane and spanwise plane in shock wave and boundary layer interactions flow field under different incident shock wave intensities. The velocity field was also analyzed. Quan *et al.* (2014) studied the fine structure of interference flow field under different boundary layer states through a series of experiments. It is pointed out that the separation bubble was long and narrow when the flow boundary layer was laminar, and oval when the incoming flow boundary layer was turbulent. Wang *et al.* (2012) gave the fine structure of interference flow field under the action of micro vortex generator, believing that the flow control mechanism mainly lies in the induction control of the time-averaged structure in the upstream boundary layer. Although many achievements have been made in the research on the interference between shock wave and boundary layer, there is still much to be explored and studied on the flow mechanism.

The interaction between the shock wave and boundary layer is divided into two types according to the characteristics of shock wave. One is the interaction between steady shock wave and boundary layer, such as the interaction between incident oblique shock wave and boundary layer. The other is the interaction between unsteady shock wave and boundary layer, such as compression corner. The latter type is often encountered in engineering applications, and there are many related researches, but its flow is relatively complicated. The former type does not need to consider the influence of unsteady shock wave itself, and its flow structure is relatively simple, so it is more suitable to be used as the research object for the mechanism of shock wave and boundary layer interference.

In this paper, the interference between incident oblique shock wave and turbulent boundary layer on the wall of the wind tunnel was conducted. At present, the NPLS system can only obtain two frames of time-related images. In order to get more temporal-correlated experimental images, firstly, the NPLS system of time evolution of unsteady flow structure was explored. The stability and beam combination of multiple single-pulse lasers, the overall design and layout of CCD cameras and the synchronous and accurate control of the testing system were mainly studied. Based on this system, the experimental research on the interference between the incident shock wave of the $\theta = 15°$ shock wave generator and the turbulent boundary layer was carried out in the Ma=3.4 supersonic low-noise wind tunnel.

2. EXPERIMENTAL EQUIPMENT AND EXPERIMENTAL MODEL

2.1 Supersonic Low-Noise Wind Tunnel

The experimental research on shock wave and turbulent boundary layer interactions in this paper was carried out in the supersonic low-noise wind tunnel (shown in Fig. 1) in the Aerodynamics Laboratory of National University of Defense Technology. Due to the laboratory renovation, the wind tunnel was dismantled and the installation was resumed after renovation. Rectifying devices such as porous inverted cone and damping net are designed and installed in the settling chamber. The Kulite XCE-062-30A high-frequency pulsating pressure sensor was used to re-calibrate the freedom flow turbulence of the wind tunnel at the center of the nozzle outlet cross section in a pitot tube measurement mode.

The wind tunnel adopts the direct connection design in the structure, and there is no diamond-shaped zone in the test section, which can effectively avoid the influence of the wave to the boundary layer transition (He 2006). It is conducive to the study of the fine structure of the boundary layer transition (Quan *et al.* 2015; Zhu *et al.* 2014). The wind tunnel

is operated in an air suction mode. Upstream to the settling chamber, the gas source was the dry and clean air. The total pressure is 0.1 MPa, the total temperature is 300 K, the fluctuation levels is less than 5‰ (Liu 2015; He *et al.* 2017). The length of the test section is 550 mm, the height is 120 mm and the width is 100 mm. In order to measure the flow field of the test section from multiple directions, large-sized optical observation windows were installed on the four walls of the test section. In this experiment, the operating Mach number of the supersonic low-noise wind tunnel is 3.4, and the main parameters of the wind tunnel flow field are shown in Table 1.

2.2 Experimental Model

The experimental model used in this paper is a $\theta = 15°$ shock wave generator, and the installation of the model is shown in Fig. 2. The observation area of the flow field is shown by the red dashed box in the figure, which is the interference area between the shock wave and the turbulent boundary layer of the incoming flow on the wall of the test section. The length of the measurement plate is 250 mm. According to the measurement results of Quan *et al.* (2015), the mean velocity boundary layer thickness of the incoming turbulent boundary layer on the wind tunnel wall surface is $\delta = 11.7$ mm. In the experiment, the intersection point of the incident shock wave and the measurement bottom plate in the experimental section is taken as the origin of coordinates (*o* point), along the incoming flow direction is the direction of the *x*-axis, the vertical measurement bottom plate plane and upward direction is the positive direction of the *y*-axis, and the direction of vertical paper surface is the positive direction of the *z*-axis.

3. NPLS SYSTEM APPLIED TO TIME EVOLUTION OF UNSTEADY FLOW STRUCTURES

The schematic diagram of the NPLS system for studying the time evolution process of unsteady flow structures is shown in Fig. 3. It mainly includes four inter-line transmission type double exposure CCD cameras, a synchronous controller, multiple single pulse Nd:YAG lasers, a nanoparticle generator, and a computer system. The resolution of the CCD camera is 2048 pixels × 2048 pixels, the output image gray level is 4096, and the minimum time interval between two images is 200ns. The laser beam has a wavelength of 532 nm, a single pulse time of 6 ns, a pulse energy of 300 mJ, and a beam waist thickness of less than 1mm. TiO_2 nanoparticles were adopted as the tracers in the NPLS technique, due to its good flow-following ability in supersonic flows. For the detail description of this technique, can be seen in the paper by Zhao *et al.* (2009) Synchronous controller time control accuracy of up to 0.25 ns, far higher than CCD camera and pulse
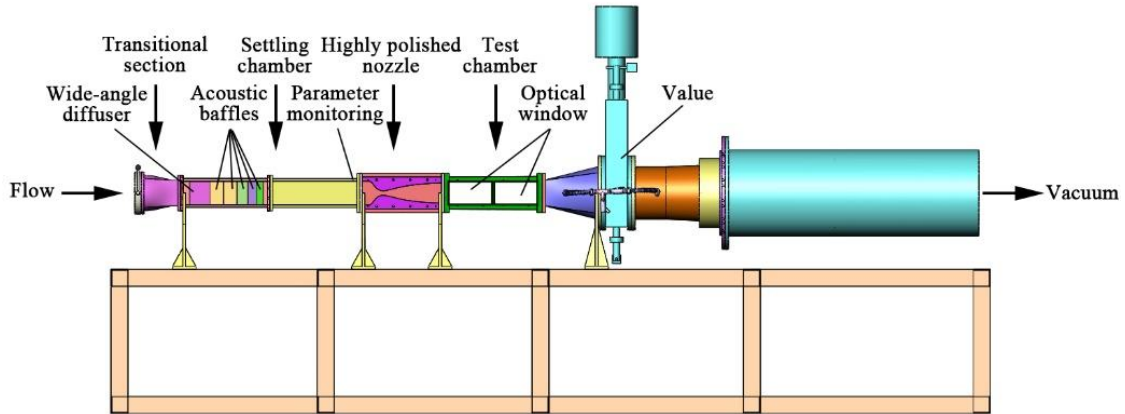
Fig. 1. Photograph of the supersonic low-noise wind tunnel.

Table 1 Flow conditions

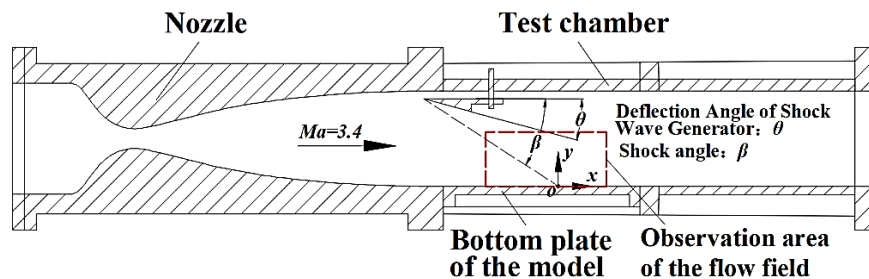| Ma_∞	P_0/MPa	T_0/K	ρ_∞/Kg•m^{-3}	U_∞/m•s^{-1}	μ/Pa•s	Re/m^{-1}
3.4	0.1	300	0.059	648.8	6.07×10^{-6}	6.30×10^6



Fig. 2. Schematic of model installation.

laser, can accurately control the synchronization of each subsystem.

Compared with the traditional NPLS system (Zhao 2008), the difference of the test system under the experimental conditions in this paper lies in the stability and beam combination adjustment after multiple single-pulse lasers are connected in parallel, the overall design and layout of the multiple CCD cameras, and the synchronous and accurate control of the test system. Before the experiment, the stability after multiple single-pulse lasers are connected in parallel is firstly explored according to the requirements. Five pulsed lasers are mainly used in this experiment. After five single-pulse lasers are connected in parallel, a photoelectric probe is arranged near the light outlet of the laser chip, in order to determine the light emitting timing sequence of each laser and test the stability of each pulse. The photoelectric probe senses the laser signal and generates an obvious step signal when the laser emits light. The operation of the synchronous controller is controlled by software, the oscilloscope is used to

collect the light emitting signals of each pulse when the laser is continuously operated and the pulse interval is set to $\Delta t=200$ns and $\Delta t=200\mu$s respectively. By comparing the time interval between two adjacent pulses, the maximum stability deviation between the pulses of the laser after parallel connection is 5 ns, which meets the requirements of the experiment. At the same time, in order to ensure that the laser slices irradiate the same flow field profile during the experiment, one pulse laser is used as the reference light source, the waist position of the slice beam is adjusted according to the size of the shooting area, and then the remaining four lasers are adjusted in sequence until each pulse laser is adjusted to combine beams. Finally, laser paper is used to detect the beam combination of the five lasers. The results are shown in Fig. 4. The deviation of the waist position coincidence degree of the viewing beam is 0.1 mm from the detection result, which does not affect the identification of the flow field structure and meets the experimental requirements.
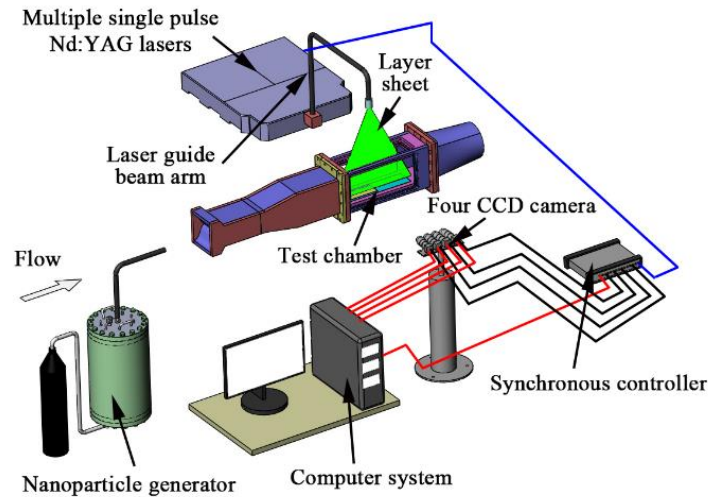
Fig. 3. Schematic of NPLS system.
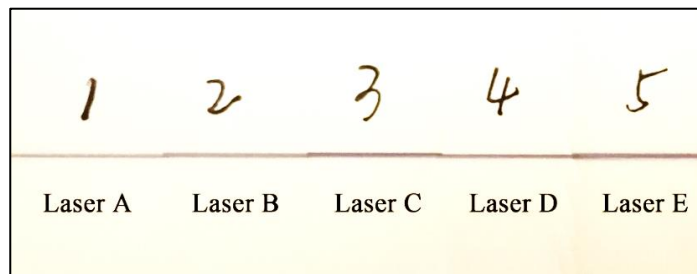
Fig. 4. Detection results of five-channel lasers beam combination.

After debugging the laser, the overall layout of the four double-exposure CCD cameras is carried out. The shooting flow range of the flow field is about 120 mm. According to the object-image relationship, lenses of the same model with a focal length of 105 mm are selected. A fine-tuning pan-tilt head is installed under each CCD camera. The deflection angle of a single camera is less than 5°. In order to calibrate the collected images, before the formal experiment, standard calibration plates are installed on the light section, and the images of the calibration plates are collected separately. The transformation matrix of each CCD camera is calculated by using the four-point calibration method. All subsequent experimental images are calibrated by the transformation matrix and then the corresponding experimental data are analyzed.

In order to coordinate the precise control of each component of the NPLS system, Fig. 5 shows the timing chart of the synchronous controller, the laser and CCD cameras. During the system working cycle, the control software instructs the synchronization controller to trigger the synchronization controller to work. The synchronization controller sends out a signal to trigger both the CCD camera 1 and the laser A at the same time. The CCD camera 1 starts the first frame exposure according to the set camera delay after receiving the trigger signal, and the laser A emits the first pulse laser through the set laser pulse delay. The first pulse laser just uniformly illuminates nanoparticles in a flow field observation area of the experimental section when the first frame of the CCD camera 1 is exposed, thus obtaining an image 1. And the subsequent CCD camera 1 continues to expose the second frame and simultaneously outputs the stored first frame image 1. Then, the lasers B, C, D and E sequentially emit the second, third, fourth and fifth pulse lasers according to a set pulse interval Δt, and the CCD camera 2, camera 3 and camera 4 will also perform exposure according to their set camera time delay to obtain image 2, image 3, image 4 and image 5. Among them, the second frame exposure of camera 1, camera 2 and camera 3 will be affected by the light intensity of the laser beam behind, and the images cannot be used, but the five-frame temporal-correlated flow field images will not be affected during the whole system working cycle. After comprehensive debugging, NPLS system for studying the time evolution process of unsteady flow structure works normally and can be used for subsequent experimental research.
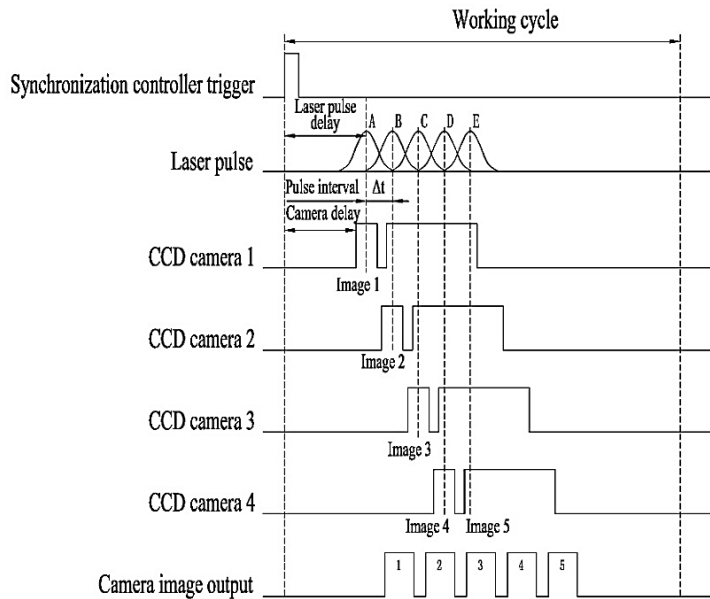
Fig. 5. Working timing diagram of NPLS system.

4. EXPERIMENTAL RESULTS AND ANALYSIS

4.1 Analysis of Fine Structure and Characteristics of SWTBLI flow Field

In order to study the development process of the wall boundary layer under the influence of the incident shock wave, the fine structure of the time evolution process of the interference between the incident shock wave and the turbulent boundary layer was measured by the NPLS technique. 180 groups temporal-correlated five-frame images can be simultaneously obtained in the one experimental running. Figs. 6 to 8 show three groups of NPLS flow visualization images respectively, and the pulse time interval is set to 12μs. The measurement range is the central surface of the wall surface, the flow direction length range is x=-70~37 mm, the spatial resolution of the image was 54.6μm/pixel, and the flow direction was from left to right. From the analysis of the NPLS image of the temporal-correlated SWTBLI in each group of images, the turbulent boundary layer structure of the incoming flow on the inner wall surface is stable at a time interval of 48μs, and there is no obvious thickness change in the boundary layer during this time interval. According to the fine structure of NPLS images in Fig. 6, Fig. 7 and Fig. 8, the thickness of the incoming flow boundary layer is δ_1=0.55δ, δ_2=0.72δ, δ_3=0.87δ respectively. The boundary layer thickness refers to the thickness obtained based on the flow display images in this experimental. Wherein the thickness is the height of the vortex structure from the wall surface, as shown in Fig. 6(a), Fig. 7(a), and Fig. 8(a), δ_1, δ_2, δ_3 was marked.

However, the flow visualization image is actually a qualitative response of the density distribution state in the flow field. And the actual thickness of the boundary layer is obtained through the change of density. Its actual physical dimension is smaller than the boundary layer thickness extracted from the velocity profile. But the thickness of density boundary layer and the thickness of velocity boundary layer are consistent in magnitude.

Based on the temporal-correlated NPLS images of SWTBLI in Figs. 6 to 8, we can clearly see the overall structure and flow development process of the wall incoming turbulent boundary layer, SWTBLI interference area flow field from the images. The time evolution process analysis was carried out for the flow structure images.

In the experiment, the turbulent boundary layer is the wind tunnel wall incoming boundary layer. When the incident shock wave acts on the wall boundary layer, due to the pressure difference between the front and back of the incident shock wave, the pressure of the incoming flow rises after passing through the incident shock wave and propagates upstream through the subsonic region inside the boundary layer and generated a reverse pressure gradient. So that the boundary layer developed and thicken rapidly, causing the boundary layer to separate and form separation bubbles. Shear is formed between the separated flow and the separation bubbles, causing the mainstream to generate a series of weak compression waves.

Based on the analysis of a large number of transient flow field images during the experiment, this series of weak compression waves converge at a certain distance from the wall surface to form induced

oblique shock waves. In addition, the unsteady forward and backward movement of shock wave and separation bubble in the boundary layer development process was induced. As the influence area of incident shock wave on the boundary layer weakened, the boundary layer on the separation wall reattached, and a fan-shaped expansion wave area

appears at the rear section of the separation bubble. After that, the airflow and the wall interact again to form a series of compression waves, which eventually converged to form a reflected shock wave, and the reattached boundary layer also returns turbulent.
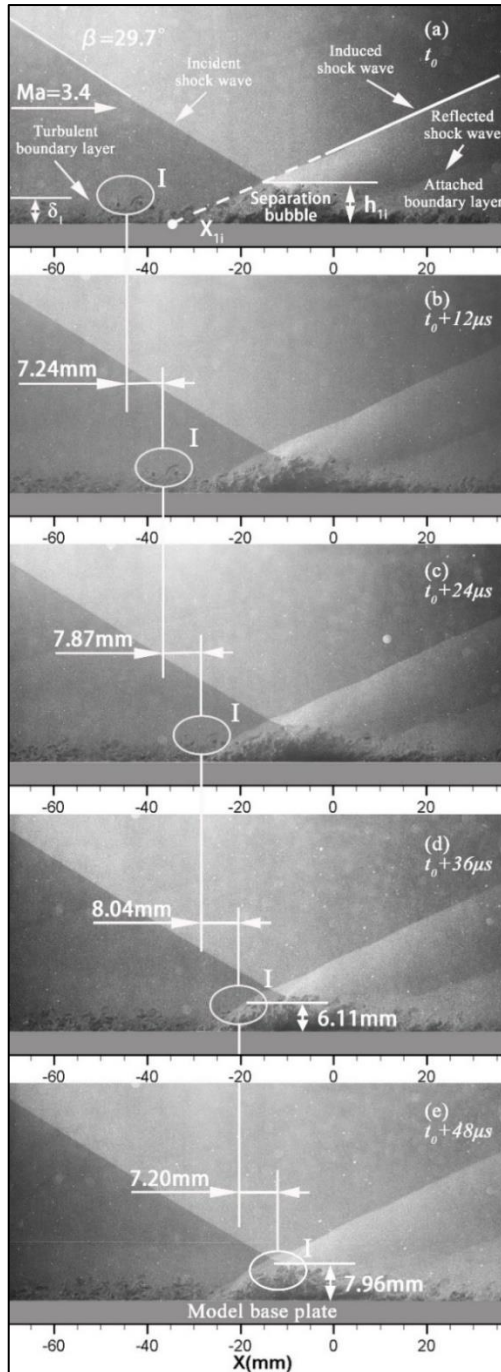

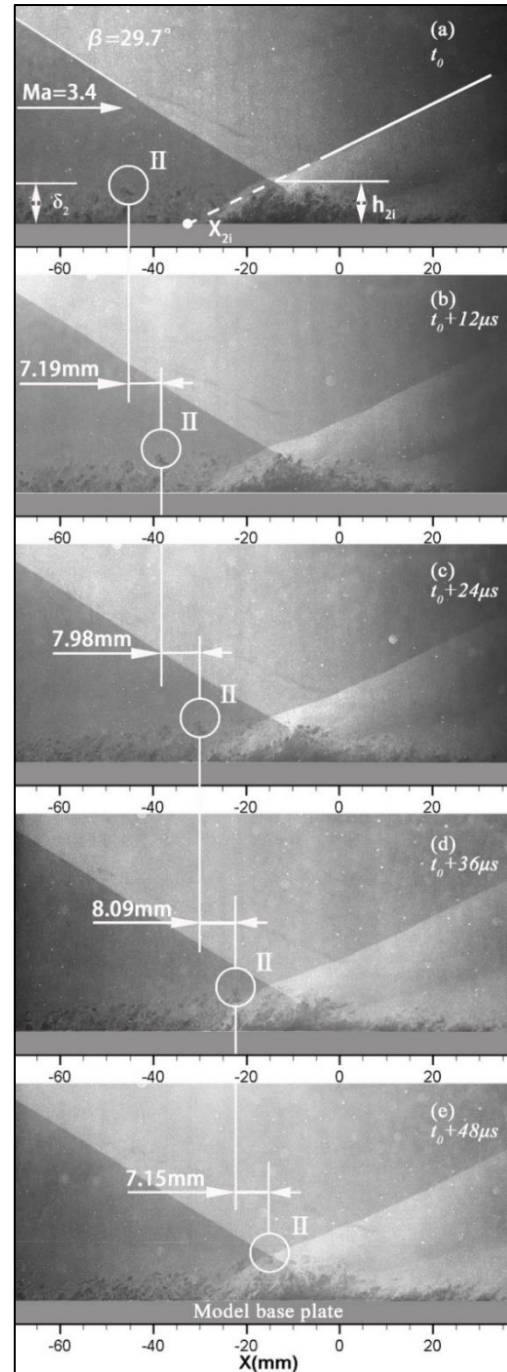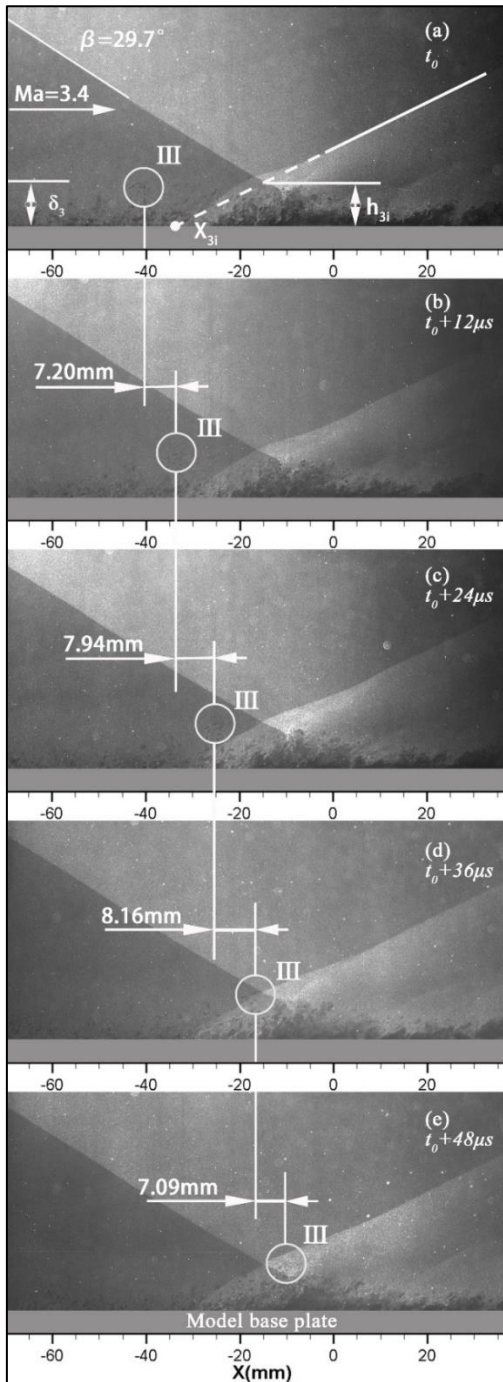**Fig. 6. NPLS images of SWTBLI in streamwise plane ($\delta_1=0.55\delta$).**

Fig. 7. NPLS images of SWTBLI in streamwise plane ($\delta_2=0.72\delta$).

Fig. 8. NPLS images of SWTBLI in streamwise plane (δ_3=0.87δ).

The vortex structure I in the turbulent region in Figs. 6 (a) to 6(e) was selected for analysis. From the five temporal-correlated images, it can be observed that the vortex structure I develops along the flow direction and enters the shock wave and boundary layer interference region and separation bubble. The displacement and motion group velocity v in the whole development process of the vortex structure I were analyzed firstly. The displacement of the vortex structure I along the flow direction was

7.24mm within Δt=0~12μs. In this paper, the reading of displacement size in image data processing is obtained by manual recognition. In the actual manual data extraction process, the error of each data point does not exceed 3 pixels. According to the spatial resolution conversion of the flow display image, the error during the manual identification and reading process can be controlled within 0.15mm, within the acceptable range inside. The streamwise group velocity of vortex structure I was about 603m/s, which was less than the mainstream velocity. It can be seen from the image that the motion of boundary layer vortex structure I was mainly translational, and the structure itself changed little. The displacement of vortex structure I along the streamwise direction was 7.87mm within Δt=12~24μs, and the calculated group velocity of vortex structure I along the streamwise direction was 657m/s, which was close to the mainstream velocity. It can also be seen from the image that the motion of boundary layer vortex structure I was still mainly translational. At this time, the vortex structure was close to the separation zone. Affected by the separation zone, the structure begins to deform and the rotation direction of the vortex packet changes slightly. The displacement of vortex structure I along the flow direction was 8.04mm within Δt = 24~36μs. The calculated velocity of vortex structure I along the flow direction group was about 670m/s, which was slightly higher than the mainstream velocity. It can be seen from the image that the vortex structure I has developed into the separation zone at this time, and the vortex packet structure has obvious deformation, but the normal displacement was very small, and the scale of the separation bubble also changes. From the analysis of the flow structure in the figure, it can be seen that the vortex structure was affected by the separation bubble motion and induced shock wave oscillation at this time, and the overall acceleration and separation bubble merge, which was equivalent to the superposition of the mainstream velocity and the overall motion velocity of the separation bubble. The group velocity of vortex structure I was slightly higher than the main flow velocity. The displacement of vortex structure I in the flow direction was 7.20mm within Δt = 36~ 48μs. The calculated group velocity of vortex structure I in the flow direction was about 600m/s, which was lower than the main flow velocity. This was due to the decrease of the flow velocity after shock wave induction. During this time, the displacement of vortex structure in the vertical direction was also 1.85 mm. The normal velocity corresponding to the vertical direction was about 154m/s, which was much smaller than the displacement in the direction of flow. From the development process of vortex structure, the vortex structure in the boundary layer enters the separation region with a certain acceleration, and the velocity decreases after completely entering the interference region, with obvious morphological changes.

In view of the unsteady motion of the induced shock wave during the interference between the shock wave and the incoming turbulent boundary layer, the oscillation interval of the induced shock wave in NPLS images of the continuous five-frame time evolution process was analyzed. The specific analysis method was shown in Fig. 6(a) by the white dashed line. The induced shock wave in the figure reversely extends along the white dashed line after passing through the intersection position of the incident shock wave and the induced shock wave. The intersection point coordinates x1i of the reverse extension line of the induced shock wave and the x-axis are obtained (i refers to the images 1, 2, 3, 4 and 5 obtained at each Δt moment). Since the intersection point position is at the intersection of the incoming boundary layer and the model wall surface, it is difficult to identify the intersection point pixel coordinates directly according to the image gray scale. In this paper, the coordinate pixel points of all intersection points xi are obtained by manually identifying and reading points, and then converted according to the image spatial resolution. The value of xi is controlled within the acceptable range in the process of extracting data from manually identified reading points. According to Figs. 6 (a) to 6(e), x_{11}=-34.54mm, x_{12}=-35.75mm, x_{13}=-34mm, x_{14}=-35.14mm, x_{15} =-32.63 mm. From the results, when the incoming flow boundary layer is δ_1=0.55δ, the oscillation range of induced shock wave in the time evolution process of Δt=12μs is about Δx_1 = 3.12mm.

At the same time, in order to analyze the growth process of the separation bubble in the time evolution process, the height dimension of the separation bubble is selected for analysis. The height of the separation bubble refers to the height of the highest point of the separation bubble structure from the bottom plate of the model. Specifically, as shown in the height mark h_{1i} in Fig. 6(a), the height dimension of the separation bubble is h_{11}=9.08mm, h_{12}=8.43mm, h_{13}=8.48mm, h_{14}=7.91mm, h_{15}=8.07mm respectively in the time evolution process of Δt=12μs according to image resolution conversion. From the results, when the incoming boundary layer is δ_1=0.55δ, the height of the separation bubble in the first frame image is slightly higher than that in the following frames, because the incoming boundary layer has not yet acted on the separation region in the first frame image, and the size of the separation bubble is affected by the cumulative effect of boundary layer time in the previous set of images. However, when the incoming boundary layer enters the separation region and acts on the separation bubble, the height of the separation bubble drops rapidly, indicating that the change of the separation bubble is greatly affected by the thickness of the incoming boundary layer.

## 4.2 Analysis of flow field characteristics of SWTBLI

In order to further analyze the unsteady motion

characteristics, the shock wave oscillation interval, vortex structure motion group velocity and separation bubble height in three sets of temporal-correlated NPLS images with the selected boundary layer thicknesses of δ_1=0.55δ, δ_2=0.72δ and δ_3=0.87δ are analyzed as a whole in this paper. The analysis method used is the same as that of Fig. 6 in 4.1. The analysis of vortex structure motion group velocity is obtained by the same algorithm as vortex structure I. The flow field characteristics of vortex structure Ⅱ and vortex structure Ⅲ in the incoming boundary layer of Fig. 7 and Fig. 8 are analyzed respectively. the induced shock wave oscillation positions are x_{2i} and x_{3i} respectively, and the separation bubble heights are h_{2i} and h_{3i} respectively in Fig. 7 and Fig. 8. The specific analysis data results are shown in Fig. 9 and Fig. 10.

Figure 9 shows the oscillation position of induced shock wave and the variation rule of group velocity of vortex structure in the boundary layer when it develops along the flow direction and enters the separation zone under the selected three incoming boundary layer thickness conditions. It can be seen from the figure that although the incoming boundary layer thickness changes, the group velocity in the development process of vortex structure has not changed greatly. The group velocity of vortex structure is lower than the mainstream velocity in the position far away from the separation zone, and there is an acceleration process when approaching the separation bubble. When the velocity reaches its maximum, the group velocity is close to the mainstream velocity. During this process, the change of vortex structure itself is small, and the velocity decreases rapidly after the vortex structure completely enters the separation bubble. However, for boundary layers with different thicknesses, there are differences in the interval of shock wave oscillation induced in the time-dependent image sequence. When the boundary layer thickness is δ_1=0.55δ, the x_{1i} oscillation interval is -35.75 mm to-32.63 mm, with the range of Δx_1 = 3.12 mm; When the boundary layer thickness is δ_2=0.72δ, the x_{2i} oscillation interval is -33.88mm~-32.46mm, with a range of Δx_2 = 1.42mm; When the boundary layer thickness is δ_3=0.87δ, the x_{3i} oscillation range is -34.37mm~-31.32mm, and the range is Δx_3 = 3.05 mm. From the results, for three different boundary layer thicknesses, the variation of shock oscillation range is not obvious during the time evolution process, which may be related to the limited number of samples. However, for the same incident shock and the incoming turbulent boundary layer, the whole range of shock oscillation is closer to the center of the separation bubble as the thickness of the incoming turbulent boundary layer increases.

Figure 10 shows the distribution and variation law of separation bubble height h under three incoming boundary layer thicknesses. from the figure, it can be seen that the structural dimension variation of separation bubble is also different for different

incoming turbulent boundary layer thicknesses. For boundary layer thickness $\delta_1=0.55\delta$, after the incoming vortex structure develops to the action zone, the height dimension of separation bubble does not change obviously, which is influenced by the relatively thin incoming boundary layer thickness. After the incoming vortex structure enters the separation region, the size of the separation bubble structure tends to decrease. For boundary layer thicknesses $\delta_2=0.72\delta$ and $\delta_3=0.87\delta$, the height of the separation bubble tends to be stable before the incoming vortex structure enters the separation region. As the incoming vortex structure enters the separation region, the size of the separation bubble increases significantly. The higher the thickness of the incoming boundary layer, the higher the overall growth height of the separation bubble. This also shows that the thickness of the incoming turbulent boundary layer has certain influence on the unsteady motion law of the induced shock wave and the change of the separation bubble size in the separation region.
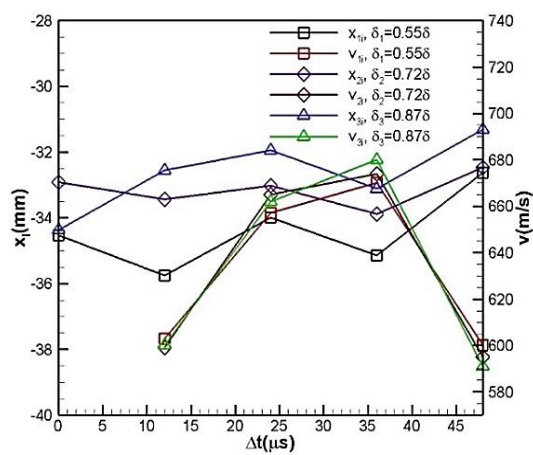
Fig. 9. Trajectory of induced shock wave and velocity of vortex structure motion group.
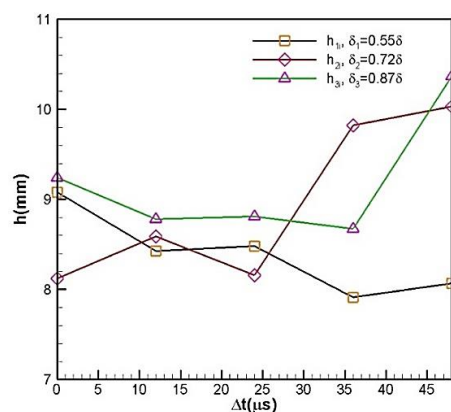
Fig. 10. Height of separation bubble.

5. CONCLUSION

In this paper, the time evolution NPLS system of unsteady flow structure was first finished. The stability and beam combination of multiple single-pulse lasers connected in parallel, the overall design and layout of array CCD camera and the synchronous and accurate control of the testing system were mainly studied. After five single-pulse lasers were connected in parallel and the optical path adjusting device was used, five stable and beam-combined pieces of light are obtained. By designing the layout mechanism of the array camera and adjusting the pan-tilt, the CCD camera with similar shooting areas was obtained. By analyzing the time sequence of the whole system, measuring and debugging the time delay of each subsystem, the accurate control of the whole testing system can be achieved. And the experimental research on the interactions between the incident shock wave of the $\theta = 15°$ shock wave generator and the turbulent boundary layer on the incoming flow wall was carried out in the Ma=3.4 supersonic low-noise wind tunnel, and the following conclusions were obtained:

(1) The NPLS system exploration research on the time evolution of unsteady flow structure has obtained five frames temporal-correlated fine structure images of SWTBLI flow field under experimental conditions for the first time, and the time-space evolution process of flow structure in SWTBLI process was analyzed.

(2) The flow field characteristics of SWTBLI were analyzed through temporal-correlated images of different incoming turbulent boundary layer thicknesses. It is concluded that for the same incident shock wave, and with the increase of the incoming boundary layer thickness, the group velocity in the development process of vortex structure in the turbulent boundary layer does not change significantly, but the overall interval of shock wave oscillation is closer to the center of the separation bubble.

(3) When the thickness of the incoming turbulent boundary layer is small, the height dimension of the separation bubble does not change obviously, and the height of the separation bubble tends to decrease. When the thickness of the incoming turbulent boundary layer is relatively large, the size of the separation bubble increases obviously, and when the thickness of the incoming turbulent boundary layer is larger, the overall growth height of the separation bubble also increases.

REFERENCES

Ackeret, J. F. Feldmann and N. Rott (1947). Investigations of Compression Shocks and Boundary Layers in Gasses Moving at High Speed. *NACA TM 1113*.

Adamson, T. C. and A. F. Messiter (1980). Analysis of two-dimensional interactions between shock waves and boundary layers. *Annual Review of Fluid Mechanics* 12, 103-138.

Andreopoulos, J. and K. C. Muck (1987). Some new aspects of the shock-wave/boundary-layer interaction in compression-ramp flows. *Journal of Fluid Mechanics* 180, 405-428.

Delery, J. and J. G. Marvin (1986). Shock-wave boundary layer interactions. *AGARDograph 280*.

Dolling, D. S. (2001). Fifty years of shock wave/boundary layer interaction research: what next? *AIAA Journal* 39, 1517-1531.

Donaldson, C. and P. Du (1944). Effects of interaction between normal shock and boundary layer. *NACA CB 4A27*.

Dupont, P., C. Haddad and J. F. Debieve (2006). Space and time organization in a shock-induced separated boundary layer. *Journal of Fluid Mechanics* 559, 255-277.

Fage, A. and R. F. Sargent (1947). Shock Wave and Boundary Layer Phenomena Near a Flat Surface. *Proceedings of The Royal Society A*, 190, 1-20.

Ferri, A. (1939). Experimental results with airfoils tested in the high speed tunnel at Guidonia. *NACA TM 946*.

Green, J. E. (1970). Interactions between shock waves and turbulent boundary layers. *Progress in Aerospace Sciences* 11, 253-340.

Hankey, W. L. and M. S. Holden (1975). Two-dimensional shock-wave boundary layer interactions in high-speed flows. *AGARDograph 203*.

He, L. (2006). *The design and experimental studies of supersonic straight through wind tunnel and supersonic-supersonic mixing layer wind tunnel.* Master thesis. National University of Defense Technology, Changsha, Hunan, China.

He, L. (2011a). *Experimental investigation of supersonic boundary layer and shock wave/boundary layer interaction*. Ph. D. thesis. National University of Defense Technology, Changsha, Hunan, China.

He, L., S. H. Yi and X. G. Lu (2017). Experimental study on the density characteristics of a supersonic turbulent boundary layer. *Acta Physica Sinica* 66.

He, L., S. H. Yi., Y. X. Zhao, L. F. Tian and Z. Chen. (2011b). Visualization of coherent structures in a supersonic flat-plate boundary layer. *China Science Bulletin* 56, 489-494.

John, B. and P. Senthilkumar (2018). Alterations of Cowl Lip for the Improvement of Supersonic-Intake Performance. *Journal of Applied Fluid Mechanics* 11(1), 31-41.

Liepmann, H. W. (1946). The Interaction between Boundary Layer and Shock Waves in Transonic Flow. *Journal of Aerospace Sciences*. 13, 623-638.

Liu, X. L. (2015). *The hypersonic low noise wind tunnel technique and relative experimental studies*. Master thesis. National University of Defense Technology, Changsha, Hunan, China.

Lu, X. G., S. H. Yi, L. He, X. L. Liu and H. B. Niu. (2020). Experimental Investigation of the Hypersonic Boundary Layer Transition on a 45° Swept Flat Plate. *Fluid Dynamics* 55, 111-120.

Pirozzoli, S. and F. Grasso (2006). Direct numerical simulation of impinging shock wave/turbulent boundary layer interaction at M=2.25. *Physics of Fluids* 18, 065113.

Quan, P. C., S. H. Yi, Y. Wu, Y. Z. Zhu and Z. Cheng. (2014). Experimental investigation of interactions between laminar or turbulent boundary layer and shock wave. *Acta Phys.* 63(8), 084703.

Quan, P. C., S. H. Yi, Y. Wu, Y. Z. Zhu and L. He. (2015). Experimental Investigation on the Effects of Swept Angles on Blunt Fin-Induced Flow. *AIAA JOURNAL*.

Singh, N. K. (2019). Instability and Transition in a Laminar Separation Bubble. *Journal of Applied Fluid Mechanics* 12(5), 1511-1525.

Smits, A. J. and J. P. Dussauge (2006). *Turbulent Shear Layers in Supersonic Flow*, 2nd editon. Springer, New York.

Tong, F. L., D. Sun, X. X. Yuan and X. L. Li. (2020). Direct numerical simulation of impinging shock wave/ turbulent boundary layer interactions in a supersonic expansion corner. *Acta Aeronautica Sinica*.

Wang, B., W. D. Liu, Y. X. Zhao, X. Q. Fan and C. Wang. (2012). Experimental investigation of the micro-ramp based shock wave and turbulent boundary layer interaction control. *Physics of Fluids* 24, 055110.

Wu, M. and M. P. Martin (2008). Analysis of shock motion in shockwave and turbulent boundary layer interaction using direct numerical

simulation data. *Journal of Fluid Mechanics* 594, 71-83.

Yao, Y. and B. Gao (2019). Flow structure of incident shock wave boundary layer interaction with separation. *Acta Aerodynamica Sinica*, 37(5), 740-747,769.

Zhang, Y., H. J. Tan, Z. Y. Wang, X. Li and B. J. Guo. (2020). Progress of Shock Wave/Boundary Layer Interaction and Its Control in Inlet. *Journal of Propulsion Technology* 41(2), 241-259.

Zhao, Y. X. (2008). *Experimental investigation of spatiotemporal structures of supersonic mixing layer.* Ph. D. thesis. National University of Defense Technology, Changsha, Hunan, China.

Zhao, Y. X., S. H. Yi, L. F. Tian, and Z. Y. Cheng. et al (2009). Supersonic Flow Imaging via Nanoparticles. *Science in China Series E* 52, 3640.

Zhao, Y. X., S. H. Yi, L. He, Z. Y. Cheng and L. F. Tian. (2007). The experimental study of interaction between shock wave and turbulence. *China Science Bulletin* 52, 1297-1301.

Zhu, Y. Z., S. H. Yi, X. P. Kong P. C. Quan, Z. Chen and L. F. Tian. (2014). Fine structures and the unsteadiness characteristics of supersonic flow over backward facing step via NPLS. *Acta Phys*. 63(13), 134701.